

Five decades of northern land carbon uptake revealed by the inter-hemispheric CO₂ gradient

P. Ciais ^(1,2), **J. Tan** ⁽²⁾, **X. Wang** ⁽²⁾, **C. Roedenbeck** ⁽³⁾, **F. Chevallier** ⁽¹⁾, **S-L. Piao** ^(2,4), **R. Moriarty** ⁽⁵⁾, **G. Broquet** ⁽¹⁾, **C. Le Quéré** ⁽⁵⁾, **J.G. Canadell** ⁽⁶⁾, **S. Peng** ⁽²⁾, **B. Poulter** ⁽⁷⁾, **Z. Liu** ^(8,9), and **P. Tans** ⁽¹⁰⁾.

- [1] Laboratoire des Sciences du Climat et de l'Environnement, CEA-CNRS-UVSQ, F-91191, Gif sur Yvette, France
- [2] Sino-French Institute for Earth System Science, College of Urban and Environmental Sciences, Peking University, Beijing 100871, China
- [3] Max Planck Institut für Biogeochemie, P.O. Box 600164, Hans-Knöll-Str. 10, 07745 Jena, Germany
- [4] Institute of Tibetan Plateau Research, Chinese Academy of Sciences, Beijing 100085, China
- [5] Tyndall Centre for Climate Change Research, University of East Anglia, Norwich NR4 7TJ, UK
- [6] CSIRO Oceans and Atmosphere, GPO Box 1700, Canberra ACT 2601, Australia
- [7] NASA Goddard Space Flight Center, Biospheric Sciences Lab, Greenbelt, Maryland 20771, USA
- [8] Resnick Sustainability Institute, California Institute of Technology, Pasadena, California 91125, USA
- [9] John F. Kennedy School of Government, Harvard University, Cambridge, Massachusetts 02138, USA
- [10] NOAA Earth System Research Laboratory, Boulder, CO 80305, USA

Multiple lines of evidence^{1,2} have established the existence of a land carbon sink in the northern hemisphere, but its trend remains poorly understood^{3,4}. Here we show from measurements of the atmospheric CO₂ gradient between the stations of Mauna Loa (north) and of South Pole (south) since 1958 that the northern land sink remained rather stable between the 1960s and the late 1980s, but increased by 0.5 ± 0.4 Pg C yr⁻¹ during the 1990s and further by 0.6 ± 0.5 Pg C yr⁻¹ during the 2000s. The first increase of the northern land sink in the 1990s accounts for 65% of the increase in the global land flux during that period. The subsequent increase in the 2000s is larger than the increase of the global land flux, suggesting a coincident decrease of carbon uptake in southern regions. The decadal change in the northern land sink between the 1960s and the 1990s can be explained with a combination of rising atmospheric CO₂, climate variability, and changes in land-cover as represented in an ensemble of terrestrial carbon cycle models⁴. The increase during the 2000s is however underestimated by all terrestrial models. Reducing uncertainties involve better consideration of changes in drivers such as land use change, diffuse light, and nitrogen deposition as well as denser observations to clarify the importance of different regions.

Fossil fuel and land-use change emissions of CO₂ into the atmosphere increased by a factor of three between 1960 and 2016, with a fast growth rate in the 1980s, a slower growth rate in the 1990s and a re-acceleration⁵ in the 2000s. The global land and ocean carbon sinks increased proportionally with growing emissions⁶ but their location and trends are incompletely understood. Northern Hemisphere (NH) lands make a dominant contribution to the global land carbon sink^{1-4,7-8}. In the NH mid and high latitudes, vegetation greenness increased in the last 30 years⁹, and the seasonal amplitude of CO₂ increased by 50% in the last 50 years¹⁰, suggesting an enhancement of ecosystem production. However, these observations are not proofs that the NH net carbon sink is increasing because of possible upward trends in soil respiration¹¹ and land-use emissions compensating for increased production.

To gain insights on the long-term trend in the northern land sink over the last 50 years, we use the inter-hemispheric gradient of atmospheric CO₂ (IG) defined as the observed difference of atmospheric CO₂ between the Mauna-Loa (MLO) station located at 19°N, and South Pole (SPO). Both MLO and SPO record CO₂ growth rates representative of the means in their respective hemisphere¹². Here we examine the relationship between IG and fossil fuel and cement CO₂ emissions (F) between 1958 and 2016, and recent changes during the 2000s, a period marked by the acceleration of global CO₂ emissions, mainly from East and South Asia regions¹³⁻¹⁴.

From 1958 to 2016 the IG grew proportional to F (Fig. 1; Fig. ED1) with a Pearson correlation coefficient (*r*) of 0.97 (*p* < 0.01) and a mean regression slope¹⁵ of 0.44 ± 0.01 ppm per PgC yr⁻¹ (Methods) This tight IG-F linear relationship is an important property of the carbon cycle perturbed by human activities¹⁶. It implies that the carbon sink difference between the NH and the Southern hemisphere (SH) has increased and kept pace with the upward trend of F (Methods; Fig ED1). Between the 1960s and the last decade (2007-2016) the increase of F alone would imply an increase of IG of 4.4 ± 0.2 ppm (Methods) while observed IG increased only by 3.9 ± 0.08 ppm. Thus, even if the relationship shown in Fig. 1 is dominated by the increase of F it cannot be all explained by it. The increasing North-South difference of carbon sinks implied by the data in Fig. 1 could reflect trends either in the Northern or in the Southern Hemisphere. A persistent reduction of the Southern Ocean uptake over 50 years as the sole explanation for the IG-F relationship shown in Fig. 1 is implausible. A sustained decrease of the Southern Ocean sink at a mean rate of 0.6 PgC yr⁻¹ per decade would be needed, which is inconsistent with the small weakening¹⁷ during 1981-2002 and its strengthening thereafter¹⁸. A declining sink or increasing source in southern terrestrial ecosystems is

also unlikely because most southern hemisphere forests are close to the equator, so that a trend in their CO₂ balance has only a weak effect on IG. In addition, declining carbon accumulation in tropical forests biomass over the Amazon¹⁹ (in the last 2 decades and here extrapolated to the last 5 decades) or increasing southern hemisphere land use change emissions²⁰ are too small to explain the data presented in Fig. 1. The most plausible hypothesis is that an increasing trend in the NH land and ocean fluxes explains the observed trends of IG.

Decadal variability is superimposed on the long-term linear trend of IG. In the late 1990s, IG was above the linear fit defined by all the years (Fig. 1) whereas during the 2000s, IG dropped below the fit line ($p < 0.01$) and returned back close to it after 2010. The IG-F linear regression slope calculated from MLO decreased by 0.5 ppm per PgC yr⁻¹ between the period going from the early 1980s to 1999 (period 1) and the following period from 2000 to 2009 (period 2). The IG-F linear regression slopes calculated from seven long-term NH atmospheric CO₂ stations with at least 20 years of measurements (Methods) exhibit decadal changes consistent with those observed at MLO (Fig. ED2). Figure 2 shows IG-F slopes from these NH stations for period 1 and period 2. Between these two time-periods, the IG-F slope decreased at the 7 stations (Fig 2; Tables ED1 and ED2). We examine below possible explanations for this decreased sensitivity of IG to F during the 2000s.

In the 1960s, the largest fraction (75%) of global fossil fuel and cement emissions was in Europe and North America. In the 2000s, these two regions accounted for only 45% of F while the rest was in Asia. In the last two decades, F increased predominantly in East and South Asia, closer to the Western Pacific Inter Tropical Convergence Zone (ITCZ) and the Asian monsoon convergence zone (Fig. ED3) where CO₂ emitted at the surface is uplifted by convection and transported across the equator towards the SH²¹. This southward and eastward shift of F leads us to expect a decrease of the IG-F slope in the 2000s at northern mid-latitude stations in North America and Europe, paralleled with an increase at located in the Western-Pacific and close to East Asia.

We simulated the distribution of a fossil fuel CO₂ tracer with two different transport models, LMDZ²² and TM3²³ between 1979 and 2013. Both models were prescribed with inter-annual wind fields (two different fields for TM3) and geographically variable emissions (Methods). The result of these simulations gives a strong linear relationship between IG_{mod}^F and F at all northern stations, where IG_{mod}^F is the modeled inter-hemispheric gradient of the fossil fuel CO₂ tracer. The two TM3 simulations show only a small decrease in the simulated IG_{mod}^F -F slopes (Fig. ED3) during the 2000s compared to the previous decades, well below the observed decrease of the IG-F slope. The LMDZ simulation shows almost no change in IG_{mod}^F -F slope. From this, we conclude that the increase of F

in Asian regions closer to the ITCZ accounted less than 5% of the observed diminution of IG-F slopes in the 2000s. This small contribution is further supported by the fact that during 2010-2014, IG returned to values close to those defined by the long-term mean IG-F regression (Fig. 1) whereas emissions from Asia continued to stay high.

A second mechanism that can explain the lower than normal IG values relative to F in the 2000s is an increase of the NH minus SH sink difference. We applied a 2-box inversion model to diagnose changes in the NH land sink (L_N) from observations of IG and of the CO₂ growth rate over the last 5 decades. The northern land sink is given by:

$$L_N = \frac{1}{2} [(F_N - F_S) + L - (O_N - O_S) - 2\alpha\tau^{-1}IG] \quad (1)$$

The sign convention is positive for F and negative for sinks, and we used $-L$ and $-O$ for land and ocean sinks to present positive values for sinks (a very small term with the growth rates difference in both hemispheres is not reported in Equation 1 for simplicity but was included in the 2-box inversion, see Methods). L is the global land flux including land use emissions, and it is deduced from the global CO₂ budget equation, $O_N - O_S$ the ocean sink inter-hemispheric difference, α a conversion factor²⁴ and τ the inter-hemispheric CO₂ mixing time set to 1.4 years²⁵. For annual $O_N - O_S$ we used the mean value from seven ocean models driven by rising CO₂ and variable climate¹³ during the last 50 years (uncertainty from their 1-sigma standard deviation; Fig. ED4).

Between 1959 and 2013, we found that L_N is an average sink of 1.4 ± 0.4 PgC yr⁻¹ and a sink each individual year. L_N shows an average positive trend of 0.3 ± 0.2 PgC yr⁻¹ per decade (Mann Kendall test; $p < 0.05$) nearly identical to the positive trend of L . The fact that L_N increased at the same rate than L suggests that the SH land flux remained stable over time. Fig. 3 shows a net increase of L between 1989 and the 1994 followed by oscillations until a continuously large land sink prevailed after the mid-2000s. There was an increasing trend of L_N ($p < 0.05$) coincident with this increase of L (Fig 3). Between the 1960-1990 and the 1990s, L_N increased by 0.5 ± 0.4 PgC yr⁻¹ and L increased by 0.9 PgC yr⁻¹. The increase of L_N in the 1990s thus accounted for 65% of the global increase in L (Table ED3). Between the 1990s and the 2000s, L_N increased by 0.6 ± 0.5 PgC yr⁻¹ and L increased only by 0.4 ± 0.6 PgC yr⁻¹ (Table ED3) implying either a weaker land carbon uptake in the SH by 0.2 PgC yr⁻¹ - roughly consistent with available forest inventories data^{8,19} - or a weaker southern ocean sink - not confirmed by ocean models¹³ and data-driven modeled estimates^{26,27}. Similar results were also found when $O_N - O_S$ is from data-driven models^{26,27} after the mid 1980's instead of from ocean models (Fig. ED4).

F grew by 0.9 PgC yr⁻¹ between the 1980s and the 1990s, and by 1.5 PgC yr⁻¹ between the 1990s and the 2000s. In the face of this increased forcing of the carbon cycle, the ratio L_N / F does not show significant change between any of the last five decades, ranging from a minimum of 0.21 in the 1980s to a maximum of 0.27 in the 2000s. Arguably, the 2-box inversion of L_N has systematic uncertainties due to assumptions that MLO and SPO represent hemispheric-mean CO₂ concentrations, and aggregation of atmospheric transport and surface fluxes. Over the period of 1979-2013, we compared L_N with the results of two other inversions^{28,29}, MACC and JENA (CarboScope) based on 3D transport models solving for weekly fluxes in each grid cell of the globe and using CO₂ records from > 100 stations (Methods). Within their relative uncertainties, JENA and the 2-box inversions produce L_N values that are consistent with each other (R=0.92; Fig. S8). MACC and the 2-box inversion have consistent L_N variations (R = 0.77; Fig. ED5) but the decadal L_N of MACC is higher than the 2-box inversion in the late 1980s and early 1990s (Fig. 4). Overall, this suggests that the 2-box inversion, despite its simplicity, accounts for both the mean value and the variations of L_N .

In the 2-box inversion, the inter-hemispheric atmospheric mixing time τ was fixed at 1.4 ± 0.2 years from ref. 21. One difficulty in assessing possible temporal variations of τ is that it depends on the air mass exchange convoluted with spatiotemporal emission patterns of each tracer, which the 2-box model cannot resolve. Sulfur hexafluoride (SF₆), a tracer emitted only by anthropogenic activities and measured at long-term stations (<http://agage.mit.edu>) can be used as a proxy of fossil fuel CO₂ to bring insights on possible changes of τ ^{3,25}. During the period 1996-2008, changes in the IG gradient of SF₆ were dominantly explained (60%) by a southward displacement of SF₆ emissions, and to a lesser extent (40%) by a decreasing inter-hemispheric mixing time (τ_{SF_6}) according to ref. 25. We constructed an extreme scenario for the 2-box inversion assuming that τ for CO₂ decreased linearly at the same rate than τ_{SF_6} during the entire period 1990-2010. This scenario produces a smaller increase of L_N compared to constant τ , and gives an increase of L_N of 0.4 ± 0.5 PgC yr⁻¹ between the 1990s and the 2000s, i.e. 73% of the increase obtained with constant τ (Fig ED5). From this, we conclude that up to 30% the magnitude of the decadal shift of L_N in the 2000s might be explained by a decreasing τ . More complex trends in atmospheric transport, not modeled in the 2-box inversion, could also bias the inferred L_N , in particular trends in the so-called atmospheric transport rectifier effect³⁰. Using the TM3 transport model, we addressed this question and verified that ‘rectifier trends’ related to the co-variation between trends in seasonal transport and trends in of de-seasonalized land fluxes, did not produce any trend in IG, thus being no source of systematic error in the 2-box inference of L_N (Fig. ED6).

Finally we compare the time series of L_N in Fig. 3 with the simulations of terrestrial carbon models over the same period (Table ED3 and Fig. ED7). We use the results from 9 models^{4,13} (TRENDY-V4) that include land cover change, fire, climate change and CO₂ fertilization effects. Three of these models represent carbon-nitrogen (C-N) interactions, which can either limit or enhance carbon sinks, the latter over temperate regions where most nitrogen deposition occurs. The mean of terrestrial carbon models gives a northern land sink $L_{N\ mod}$ on average lower than L_N from the 2-box inversion during any decade (Fig. 4 and Table ED1). From the simulations without land use change (Fig. 4) $L_{N\ mod}$ is a bit larger because land use in the NH was dominated by agricultural abandonment causing carbon sequestration, but still below the 2-box inversion. The mean $L_{N\ mod}$ has a higher temporal year-to-year correlation ($R = 0.79$) with L_N than any individual model. Between the 1980s and the 1990s, all models produce an increase of $L_{N\ mod}$ of the same magnitude than the observed in the 2-box inversion (0.4 ± 0.2 PgC yr⁻¹). Between the 1990s and 2000s however, the models do not reproduce the observed increase of L_N (Table ED3).

The two models representing Carbon-Nitrogen (N) interactions and driven by variable N-deposition simulate in the 2000s an increase of $L_{N\ mod}$ (0.2 to 0.3 PgC yr⁻¹) at the lower end of the observed increase from inversions (0.2 to 0.6 PgC yr⁻¹). In contrast, four of the five models without C-N interactions did not reproduce any intensification of $L_{N\ mod}$ (Table ED3 and Fig. ED7). No conclusion can be drawn from a sample of two models about the role of increased nitrogen deposition, and the difference of the increase in $L_{N\ mod}$ between C-N models and C only models is not significant.

More than two decades ago, Tans *et al.*¹ inferred a large northern land sink while Keeling *et al.*² explained most of the northern sink by ocean uptake. Since then, multiple streams of evidences confirmed the existence of a persistent land carbon sink. The long-term average value of this sink inferred here from the longest atmospheric CO₂ records is higher than the results of terrestrial carbon cycle models. Terrestrial models capture the inter-annual variability of L_N well but underestimate the recent increase of L_N in the 2000s. They might under-estimate the recent effect of increased N-deposition³¹ over Chinese and Siberian forests given that the fertilizing effects of nitrogen on forest growth are larger at low exposure levels³². Additional drivers not included in models are increasing diffuse light fraction from aerosols scattering effects over East Asia³³ and expanding young forests and plantations in this region as well. This study underscores the need for a coordinated stewardship of the northern land sink as part of the climate policy agenda with the objective to maintain, and enhance whenever possible land sinks through favorable land use. It highlights the need for enhanced observations in particular over regions poorly covered by observations, Eastern Europe, Siberia and

the Arctic. It is from these far northern regions where positive and negative carbon-climate feedbacks are most likely to come in the future.

References

- 1 Tans, P. P., Fung, I. Y. & Takahashi, T. Observational Constraints on the Global Atmospheric CO₂ Budget. *Science* **247**, 1431 (1990).
- 2 Keeling, C. D., Piper, S. C. & Heimann, M. *Aspects of Climate Variability in the Pacific and the Western Americas*. Vol. 55 305-363 (AGU, 1989).
- 3 Wang, Y., Li, M. & Shen, L. Accelerating carbon uptake in the Northern Hemisphere: evidence from the interhemispheric difference of atmospheric CO₂ concentrations. *Tellus B: Chemical and Physical Meteorology* **65**, 20334 (2013).
- 4 Sitch, S. *et al.* Recent trends and drivers of regional sources and sinks of carbon dioxide. *Biogeosciences* **12**, 653-679 (2015).
- 5 Boden, T. A., Marland, G. & Andres, R. J. Global, regional, and national fossil-fuel CO₂ emissions. (US Department of Energy, Oak Ridge, Tenn., 2013).
- 6 Ballantyne, A. P., Alden, C. B., Miller, J. B., Tans, P. P. & White, J. W. C. Increase in observed net carbon dioxide uptake by land and oceans during the past 50 years. *Nature* **488**, 70 (2012).
- 7 Ciais, P. *et al.* Can we reconcile atmospheric estimates of the Northern terrestrial carbon sink with land-based accounting? *Current Opinion in Environmental Sustainability* **2**, 225-230, doi:10.1016/j.cosust.2010.06.008 (2010).
- 8 Pan, Y. D. *et al.* A Large and Persistent Carbon Sink in the World's Forests. *Science* **333**, 988-993 (2011).
- 9 Xu, L. *et al.* Temperature and vegetation seasonality diminishment over northern lands. *Nature Climate Change* **3**, 581-586 (2013).
- 10 Graven, H. D. *et al.* Enhanced Seasonal Exchange of CO₂ by Northern Ecosystems Since 1960. *Science* **341**, 1085 (2013).
- 11 Bond-Lamberty, B., Bailey, V. L., Chen, M., Gough, C. M. & Vargas, R. Globally rising soil heterotrophic respiration over recent decades. *Nature* **560**, 80-83 (2018).
- 12 Francey, R. J. & Frederiksen, J. S. The 2009-2010 step in atmospheric CO₂ interhemispheric difference. *Biogeosciences* **13**, 873-885 (2016).
- 13 Le Quéré, C. *et al.* Global Carbon Budget 2016. *Earth Syst. Sci. Data* **8**, 605-649 (2016).
- 14 Liu, Z. *et al.* Reduced carbon emission estimates from fossil fuel combustion and cement production in China. *Nature* **524**, 335 (2015).
- 15 Boggs, P. T. & Rogers, J. E. Orthogonal distance regression. *Contemporary Mathematics* **112**, 183-194 (1990).
- 16 Conway, T. J. & Tans, P. P. Development of the CO₂ latitude gradient in recent decades. *Global Biogeochemical Cycles* **13**, 821-826 (1999).
- 17 Le Quere, C. *et al.* Saturation of the Southern Ocean CO₂ sink due to recent climate change. *Science* **316**, 1735-1738 (2007).
- 18 Landschützer, P. *et al.* The reinvigoration of the Southern Ocean carbon sink. *Science* **349**, 1221 (2015).

- 19 Brienen, R. J. W. *et al.* Long-term decline of the Amazon carbon sink. *Nature* **519**, 344 (2015).
- 20 Houghton, R. A. *et al.* Carbon emissions from land use and land-cover change. *Biogeosciences* **9**, 5125-5142 (2012).
- 21 Patra, P. K. *et al.* Transport mechanisms for synoptic, seasonal and interannual SF₆ variations and "age" of air in troposphere. *Atmos. Chem. Phys.* **9**, 1209-1225 (2009).
- 22 Hourdin, F. *et al.* The LMDZ4 general circulation model: climate performance and sensitivity to parametrized physics with emphasis on tropical convection. *Climate Dynamics* **27**, 787-813 (2006).
- 23 Heimann, M. & Körner, S. Technical Report (2003).
- 24 Prather, M. J., Holmes, C. D. & Hsu, J. Reactive greenhouse gas scenarios: Systematic exploration of uncertainties and the role of atmospheric chemistry. *Geophysical Research Letters* **39**, 9 (2012).
- 25 Patra, P. K. *et al.* TransCom model simulations of CH₄ and related species: linking transport, surface flux and chemical loss with CH₄ variability in the troposphere and lower stratosphere. *Atmos. Chem. Phys.* **11**, 12813-12837 (2011).
- 26 Rödenbeck, C. *et al.* Global surface-ocean pCO₂ and sea-air CO₂ flux variability from an observation-driven ocean mixed-layer scheme. *Ocean Science* **9**, 193-216 (2013).
- 27 Landschützer, P., Gruber, N. & Bakker, D. C. E. A 30 years observation-based global monthly gridded sea surface pCO₂ product from 1982 through 2011. http://cdiac.ornl.gov/ftp/oceans/SPCO2_1982_2011_ETH_SOM_FFN. (US Department of Energy, Oak Ridge, Oak Ridge National Laboratory, Tennessee, 2015).
- 28 Chevallier, F. *et al.* CO₂ surface fluxes at grid point scale estimated from a global 21 year reanalysis of atmospheric measurements. *Journal of Geophysical Research-Atmospheres* **115**, 17 (2010).
- 29 Rodenbeck, C., Houweling, S. & Gloor, M. H., M. CO₂ flux history 1982–2001 inferred from atmospheric data using a global inversion of atmospheric transport. *Atmos Chem Phys Discuss* **3**, 2575-2659 (2003).
- 30 Denning, A. S., Fung, I. Y. & Randall, D. Latitudinal gradient of atmospheric CO₂ due to seasonal exchange with land biota. *Nature* **376**, 240 (1995).
- 31 Liu, X. *et al.* Enhanced nitrogen deposition over China. *Nature* **494**, 459 (2013).
- 32 Thomas, R. Q., Canham, C. D., Weathers, K. C. & Goodale, C. L. Increased tree carbon storage in response to nitrogen deposition in the US. *Nature Geoscience* **3**, 13-17 (2010).
- 33 Che, H. Z. *et al.* Analysis of 40 years of solar radiation data from China, 1961–2000. *Geophysical Research Letters* **32**, doi:10.1029/2004GL022322 (2005).

Acknowledgements. We acknowledge the ocean and DGVM modelers (TRENDY-V4) that provided simulations to the global carbon budget assessment in Lequeré et al. (year 2015), and the SCRIPPS

and NOAA/ERSL staff who have contributed to the collection of atmospheric data, particularly the long-term MLO and SPO records.

Authors Contributions. The study was conceived by P.C. and developed by P.C., J.T. and X.W. Simulations with the TM3 and LMDZ transport models were performed by C.R. and F. C. All other authors reviewed and provided input on the manuscript.

Author Information Reprints and permissions information is available at www.nature.com/reprints. The authors declare no competing financial interests. Readers are welcome to comment on the online version of the paper. Correspondence and requests for materials should be addressed to P.C. (philippe.ciais@lsce.ipsl.fr).

Main figure legends

Figure 1. Relationship between the inter-hemispheric gradient of CO₂ (IG) and fossil fuel CO₂ emissions (F). The solid line is an Orthogonal Data Regression fit to all years of data. The numbers next to each point are the specific years of the record. Empty circles are the results using the emissions from China from Liu *et al.* (Methods ref. 34) after year 2000 that are lower than other estimates, and the emissions from CDIAC for all other countries and international fuels. The dashed line and diamonds shows the increase of the gradient predicted with a 2-box atmospheric model from the increase of fossil fuel emissions alone.

Figure 2. Slope of linear regression fits between IG and F at long-term Northern Hemisphere atmospheric stations. a, map of selected stations (see methods). **b,** values of IG-F slopes for different periods. The circles in black are slope values during the first period (1980s and 1990s) and in red during the second period (2000s), with error bars from Orthogonal Data Regression¹⁵. Out of 11 stations, only 7 with absolute value of correlation coefficient > 0.3 are shown (Table ED1). The green star is the long-term mean slope over 1958-2016 from MLO. Fossil CO₂ emissions are from CDIAC (filled symbols) and from (Methods ref. 34) after 2000 in China combined with CDIAC for other countries (open symbols, overlaid with filled ones).

Figure 3. Global and northern hemisphere land fluxes a, Global net land flux, including land-use change (L) and other processes causing land uptake. **b,** Northern land sink (L_N) inferred from the 2-box inversion model constrained by IG measurements and the ocean sink inter-hemispheric difference from ocean models (Methods).

Figure 4. Variations in the northern land sink during the past 56 years. a, Northern land sink L_N from the 2-box inversion, the MACC and the JENA 3D inversions. Shaded areas are 1-sigma uncertainties for the 2-box inversion (Methods) and MACC. The different cyan lines represent different atmospheric networks used by the JENA inversion. **b.** $L_{N\ mod}$ from 9 land carbon cycle models driven by climate, rising CO₂ and land cover change (S3 simulation in red with shaded area being the std. deviation of the models). Results from simulation S2 without land use change in dash pink.

Methods

2-box inversion

Since no global inversion of regional CO₂ fluxes using 3D transport fields covers the past 55 years, we constructed a 2-box model to invert annual land CO₂ fluxes at the scale of the Northern and Southern Hemisphere. Let C_N be the CO₂ mixing ratio in the Northern Hemisphere (N), represented by the Mauna Loa record and C_S be the one of the Southern Hemisphere (S) represented by the South Pole record, and the annual growth rates in each hemisphere \dot{C}_N and \dot{C}_S . Given the inter-hemispheric mixing time τ , we have:

$$\alpha \dot{C}_N = F_N - O_N - L_N - \alpha \tau^{-1} (C_N - C_S) \quad (\text{M1})$$

$$\alpha \dot{C}_S = F_S - O_S - L_S + \alpha \tau^{-1} (C_N - C_S) \quad (\text{M2})$$

Where \dot{C} is the time derivative of deseasonalized CO₂ mixing ratios, F are the emissions of CO₂ from fossil fuel burning, cement production and other industrial processes, O the ocean sink and L the net land flux (including land use) counted positively if CO₂ is removed from the atmosphere, and subscripts N and S are for Northern and Southern Hemisphere, respectively. The conversion factor α between a hemispheric mixing ratio change of one ppm yr⁻¹ and the corresponding flux in PgC yr⁻¹ in one hemisphere equals 1.06 Pg C per ppm²⁴. Combining (M1) and (M2) gives:

$$IG = C_N - C_S = \frac{1}{2\alpha} \tau [(F_N - F_S) - (O_N - O_S) - (L_N - L_S) - \alpha(\dot{C}_N - \dot{C}_S)] \quad (\text{M3})$$

Equation (M3) implies that IG is proportional to the flux difference between both hemispheres if the inter-hemispheric mixing rate is constant over time. $F_N - F_S$ is from CDIAC country data with the spatial patterns of EDGARv4.2, $O_N - O_S$ from ocean model output driven by variable CO₂ and climate, being available for the period 1959-2013¹³. These are the same ocean models as those used to infer the net land flux L in the global budget equation, so that our inference of L_N from equation (M3) is consistent with the one of L . We also tested two data driven products for $O_N - O_S$ covering only the period starting from early / mid 1980s²⁶⁻²⁷ (see below). The change in IG due to fossil fuel emissions alone in Fig. 1 was calculated by setting $O_N - O_S$ and $L_N - L_S$ to zero in equation (M3) with an uncertainty of 10% for τ and 5% for F .

The shaded gray 1-sigma error range of the 2-box inversion L_N and L_S fluxes is estimated using a Monte Carlo method with 5% uncertainty in F , an uncertainty of 0.18 PgC yr⁻¹ in the CO₂ growth rates at SPO and MLO, the standard deviation of all ocean models for $O_N - O_S$ and a 10% uncertainty for τ .

Atmospheric CO₂ long-term records

Atmospheric CO₂ long-term records used in this study are from continuous in-situ measurements at the stations MLO (1958-2013) and SPO (1958-2013) from the SIO network³⁵ downloaded as monthly averages from the SIO web site (http://scrippsco2.ucsd.edu/data/atmospheric_co2.html). For months with missing data, which represent only 15% of each record, CO₂ was gap-filled using standard curve fitting algorithms³⁶ for atmospheric CO₂ data. In the early 1980s, more atmospheric CO₂ stations became available, mainly from the NOAA-ESRL network (Table ED1). We selected from the GLOBALVIEWplus CO₂ data product giving monthly smoothed CO₂³⁷ (Cooperative Global Atmospheric Data Integration Project, 2013, updated) the stations with at least 8 years during 2000-2009 and at least 12 years during 1979-1999. We further selected only the records with more than 75% of data coverage during any given month, and thus discarded stations with gaps where data from the Marine Boundary Layer composite curve is used to gap-fill CO₂ time series. This led us to retain 10 stations from the NOAA ESRL network in the NH covering the first and the second periods. Another two stations in the NH were selected from the Scripps web site (MLO, LJO). For MLO measured both by NOAA and Scripps, we used the longer Scripps record, leading to 11 long-term stations (Table ED1). The annual mean CO₂ mixing ratio was calculated from monthly smoothed data at each site to calculate the IG-F slopes. The uncertainty of IG-F slopes is estimated using a bootstrap method. We performed a linear regression analysis 1000 times by randomly selecting a subset of 80% of samples from all pairs of IG and F during 1958-2013 accounting for uncertainties in IG and F. The standard deviation of those 1000 slopes was used as the uncertainty of the slope. IG-F regression slopes are significant during both periods 1980-1999 and 2000-2009 for 7 out of 11 stations ($p < 0.01$). For 4 stations (LJO, ALT, KEY and MID) the IG-F slope correlation coefficient (r^2) is less than 0.3 during the first period. This leads to the selection of 7 long-term NH stations (BRW, STM, NWR, RYO, IZO, KUM, MLO) for IG-F slopes during both periods shown in Fig. 2. Slopes for each decade are shown in Fig. ED2.

Atmospheric 3D transport model of fossil fuel CO₂

Atmospheric simulations of fossil fuel CO₂ were performed with the global tracer transport model LMDZ²² driven by the wind analyses from the European Centre for Medium-Range Weather Forecasts⁴⁰. We use the model at the horizontal resolution 3.75° longitude × 1.9° latitude with 39 vertical layers. This version has been the default transport model of the MACC inversion system since 2014 and earlier ones have participated to various inter-comparisons within the TransCom project²⁵. In the simulation of the fossil fuel CO₂ tracer with LMDZ, emissions are from the CDIAC dataset⁵ and have the spatial pattern of emissions of EDGARv4.2 (<http://edgar.jrc.ec.europa.eu/>) with yearly

emissions in each country are scaled to the CDIAC data each year. The global total emission of CDIAC includes bunker fuels, and is thus larger than the sum of emissions from all countries. In LMDZ, yearly bunker fuel emissions are distributed using the EDGARv4.2 spatial patterns. No intra-annual variation of fossil CO₂ emissions was assumed in absence of country specific information, although the seasonality of emissions may be regionally significant³⁸.

Similar simulations were performed using the TM3 transport model²³ driven either by the NCEP³⁹ or the ERA-Interim⁴⁰ reanalysis transport fields. The model was run at the horizontal resolution 5° longitude × ~4° latitude, with 19 vertical layers (NCEP) or 26 vertical layers (ERA-Interim). Fossil fuel and cement emissions were taken from EDGAR 4.2 (with FT2010 for 2009 and 2010, extrapolation based on BP global totals for 2011 and 2012, and 2% yr⁻¹ increase afterwards). All categories provided by EDGAR 4.2 were added, except for biomass burning. The yearly emission maps were smoothly interpolated in time.

MACC inversion

We use the CO₂ inversion product²⁸ v14r2, of the Monitoring Atmospheric Composition and Climate service (MACC, <https://atmosphere.copernicus.eu/>). Since 2010, this product has been released every year, based on the assimilation of surface air sample mole fraction measurements within the LMDZ transport model²². The list of the > 130 assimilated sites is given in the Supplementary Material of ref. 41. This inversion relies on a variational formulation that estimates 8-day grid-cell (3.75° longitude × 1.9° latitude) daytime/nighttime CO₂ fluxes and the grid cell total columns of CO₂ at the initial time step of the inversion window. It allows several decades (here the 1979-2014 period) to be processed in a single assimilation window, therefore ensuring the physical and statistical consistency of the inversion over the full measurement period. The prior ocean flux is from the climatology of ref based on ΔpCO₂ observations, with no trend and no inter-annual variability. The prior ocean flux is from the climatology⁴² based on ΔpCO₂ observations, with no trend and no inter-annual variability. The prior land flux is based on a climatology from a simulation of the ORCHIDEE land surface model with no inter-annual variability, fire emissions have a priori values with inter-annual variability from GFED⁴³, and annual mean NEE over grid-cells affected by fires is forced to zero, implying full regrowth in the same year as the fires

JENA inversion

The Jena CarboScope atmospheric CO₂ inversion (version s81_v3.7) uses a set of 14 measurement stations selected to completely cover the 1981-2014 estimation period of this run. It uses individual measurements from various sampling networks, without smoothing or gap filling. Fluxes are

estimated at the grid-scale resolution (approximately 4° latitude by 5° longitude), to reduce aggregation errors. However, to counteract that the estimation would be underdetermined, spatial and temporal a-priori correlations are imposed, smoothing the estimated flux field on scales smaller than about 1 week and about 1600 km (land, in longitude direction), 800 km (land, latitude), 1900 km (ocean, longitude), or 950 km (ocean, latitude), respectively. Land flux adjustments are spatially weighted with a productivity proxy (long-term mean NPP from the LPJ model). Prior fluxes comprise anthropogenic CO₂ emissions (from EDGAR 4.2), a constant spatial flux pattern on land (time-mean NEE from the LPJ model), and a mean seasonal cycle on the ocean (from the ocean-interior inversion by ref. 44, with seasonality from ref. 45). The Jena inversion uses the TM3 global atmospheric transport model driven by meteorology from the ERA-Interim reanalysis. The optimization is performed by a single cost function minimization for the entire estimation period plus spin-up and spin-down periods⁴⁶. See <http://www.bgc-jena.mpg.de/CarboScope/> for further information and data set download.

Northern land carbon sink from land carbon models

We used the monthly land CO₂ fluxes calculated by process-based land models over the period 1959-2013. The 9 land carbon cycle models are from the TRENDYv4 project⁴, used for the independent assessment of the land sink variability in ref. 10. Each model, the common initialization and transient 20th Century simulation protocols are described in ref. 4. The majority of the land models produce a sink because they calculate a net imbalance between increasing photosynthesis (GPP) and the lagged response of ecosystem respiration (TER) in response to rising CO₂, variable climate and land-cover change (S3 simulations). Only 4 land models include fire emissions, which are part of the net land flux. One model out of 10 in the original TRENDY v4 ensemble was excluded because it gave a strong global land source (LPX). The models used are CLM4-5, JSBACH, JULES, LPJG, OCN, VEGAS, VISIT, ISAM and ORCHIDEE (Fig. ED7). Only 3 models account for C-N biogeochemical interactions and atmospheric nitrogen deposition (CLM4-5, OCN and VISIT) the latter occurring mainly over northern lands and being an additional driving force of the northern carbon sink.

Air-sea carbon flux inter-hemispheric difference from ocean biogeochemical models and from data-driven models.

Ocean biogeochemical models used over the period 1959-2013 are NEMO-PlankTOM5, NEMO-PISCES (IPSL), MPIOM-HAMOCC, MICOM-HAMOCC (NorESM-OC), NEMO-PISCES (CNRM), CSIRO and CCSM-BEC, which represents the physical, chemical and biological processes

that influence the surface ocean concentration of CO₂ and thus the air–sea CO₂ flux. The ocean CO₂ sink for each model is normalized to observations, by dividing the annual model values by their observed average over 1990–1999, and multiplying this by the observation-based estimate of 2.2 GtC yr⁻¹ as in ref. 13. We also used two data-driven models²⁶⁻²⁷ for the global time varying distribution of air-sea CO₂ fluxes is obtained by interpolation of pCO₂ data from the SOCAT database and gas exchange formulations during the past three decades, for 1985-2012 in ref. 26 and 1982-2011 in ref. 27.

Data Availability. The decadal CO₂ flux data that support the findings of this study are available in the Extended Data tables. Annual flux data from the 2-box model and other models are available at http://dods.lsce.ipsl.fr/invsat/PC/Data_yearly_NH_and_SH_land_fluxes_and_ocean_flux.xlsx. Atmospheric CO₂ data are available from the Scripps Institution for Oceanography (SIO) web site http://scrippsco2.ucsd.edu/data/atmospheric_co2.html for MLO, LJO and SPO stations and from the ESRL GLOBALVIEW-plus CO₂ open access dataset for other stations (https://www.esrl.noaa.gov/gmd/ccgg/obspack/our_products.php).

Additional references used in Methods and Extended Data

- 34 Liu, Z. *et al.* Reduced carbon emission estimates from fossil fuel combustion and cement production in China. *Nature* **524**, 335 (2015).
- 35 Keeling, C. D. & Piper, S. C. Exchanges of Atmospheric CO₂ and ¹³CO₂ with the Terrestrial Biosphere and Oceans from 1978 to 2000. (University of California, San Diego, 2001).
- 36 Thoning, K. W., Tans, P. P. & Komhyr, W. D. Atmospheric carbon dioxide at Mauna Loa Observatory: 2. Analysis of the NOAA GMCC data, 1974–1985. *Journal of Geophysical Research: Atmospheres* **94**, 8549-8565 (1989).
- 37 Masarie, K. A., Peters, W., Jacobson, A. R. & Tans, P. P. ObsPack: a framework for the preparation, delivery, and attribution of atmospheric greenhouse gas measurements. *Earth Syst. Sci. Data* **6**, 375-384 (2014).
- 38 Blasing, T. J., Broniak, C. T. & Marland, G. The annual cycle of fossil-fuel carbon dioxide emissions in the United States. *Tellus B* **57**, 107-115 (2005).
- 39 Kalnay, E. *et al.* The NCEP/NCAR 40-Year Reanalysis Project. *Bulletin of the American Meteorological Society* **77**, 437-472 (1996).
- 40 Dee, D. P. *et al.* The ERA-Interim reanalysis: configuration and performance of the data assimilation system. *Quarterly Journal of the Royal Meteorological Society* **137**, 553-597 (2011).
- 41 Chevallier, F. On the statistical optimality of CO₂ atmospheric inversions assimilating CO₂ column retrievals. *Atmos. Chem. Phys.* **15**, 11133-11145 (2015).

- 42 Takahashi, T. *et al.* Climatological mean and decadal change in surface ocean pCO₂, and net sea-air CO₂ flux over the global oceans. *Deep-Sea Research Part I-Topical Studies in Oceanography* **56**, 554-577 (2009).
- 43 van der Werf, G. R. *et al.* Global fire emissions estimates during 1997–2016. *Earth Syst. Sci. Data* **9**, 697-720 (2017).
- 44 Mikaloff Fletcher, S. E. *et al.* Inverse estimates of anthropogenic CO₂ uptake, transport, and storage by the ocean. *Global Biogeochemical Cycles* **20**, doi:10.1029/2005GB002530 (2006).
- 45 Takahashi, T. *et al.* Global sea–air CO₂ flux based on climatological surface ocean pCO₂, and seasonal biological and temperature effects. *Deep Sea Research Part II: Topical Studies in Oceanography* **49**, 1601-1622 (2002).
- 46 Rödenbeck, C. Estimating CO₂ sources and sinks from atmospheric mixing ratio measurements using a global inversion of atmospheric transport. (Max-Planck-Institut für Biogeochemie, 2005).

Legends for the Extended Data figures/tables

Figure. ED1 Evolution of the inter-hemispheric CO₂ gradient (IG) and of fossil fuel emissions. The inter-hemispheric CO₂ gradient defined by the difference in observed mixing ratios between MLO and SPO (blue) and fossil fuel and cement global CO₂ emissions from 1958 to 2013 from CDIAC (red).

Figure. ED2 Inter-hemispheric CO₂ gradient vs. emissions each decade, and gradient vs. emissions linear regression slopes in the 1980s, 1990s and 2000s. Scatter plots of the inter-hemispheric gradient (IG) vs. fossil fuel emissions (F) from CDIAC for different northern hemisphere long-term stations with sufficient data coverage (see Methods). The station of SPO is always taken as the reference to calculate IG from each station. A station is marked by asterisk if the correlation coefficient (r^2) between IG and F is higher than 0.3 during both period 1 (first available year to 1999) and period 2 (2000 to 2009). **b.** Decadal regression slopes of north-south CO₂ gradient (IG for NH stations) and F at the long-term stations for which the correlation coefficient between IG and F is higher than 0.3 during any of the last three decades. The station of SPO is taken as reference to calculate IG for each station. The slope was calculated at each site and error bars represent the ODR slope uncertainties.

Figure. ED3 Fossil fuel emissions shift in latitude and longitude each decade and Simulated IG-F slopes in 1980s-1990s and in the 2000s with three different atmospheric transport models. **a.** Fraction of northern global fossil CO₂ emissions in each latitude band and in each longitude band during 1980-2013. **b.** Slope of Orthogonal Least Square linear regressions between modeled IG for a simulated fossil fuel CO₂ tracer (see Methods) and fossil CO₂ emissions. Three global 3D transport models were used with inter-annual winds to obtain these results (Methods), namely LMDZ with ERA-Interim ECMWF winds, TM3 with ERA-Interim ECMWF winds, and TM3 with NCEP winds. LMDZ and TM3 were prescribed time varying F maps. The modeled distribution of the fossil fuel CO₂ tracer in the atmosphere has been sampled at the location of each long-term station. The slopes are shown for two periods: \approx 1980-1999 (where \approx 1980 is the first year of observations at each site) and 2000-2009. The modeled fossil fuel CO₂ tracer at SPO is taken as reference to calculate IG at all sites.

Figure. ED4. Ocean flux differences between northern and southern hemisphere, from ocean biogeochemical models, data-driven models and inversions. **a.** Inter-hemispheric difference of ocean fluxes ($O_N - O_S$) from the seven ocean models used in Le Quéré *et al.* between 1959 and 2013. **b.** Estimates of ($O_N - O_S$) from MACC and JENA inversion results over the period they cover, and from the two ocean data-driven models described in Methods. **c.** Northern land flux (L_N) inferred from the 2-box inversion with ($O_N - O_S$) being the mean value from seven ocean models, and from each of the two data driven models, respectively.

Figure ED5. Northern land sink from inversions with decadal mean values and northern land sink sensitivity to inter-hemispheric mixing time. **a.** Northern land sink from the 2-box inversion (black with 1-sigma uncertainty in gray) and from MACC and JENA 3D inversions. In the 3D inversions, L_N is calculated by summing the flux of land grid cells north of the Equator. Numbers indicate decadal mean values and numbers in brackets the change in L_N from one decade to the next. **b.** Comparison of L_N inferred by the 2-box inversion in the control case (black) where the inter-hemispheric mixing time is set constant at 1.4 years and in a scenario (red) where it is inferred from SF₆ measurements (see text) to have decreased linearly by 0.57 % yr⁻¹ from 1990 to 2013,

corresponding to the decrease not explained in Patra *et al.* (ref. 21) by a southward shift in geographic distribution of SF₆ emissions.

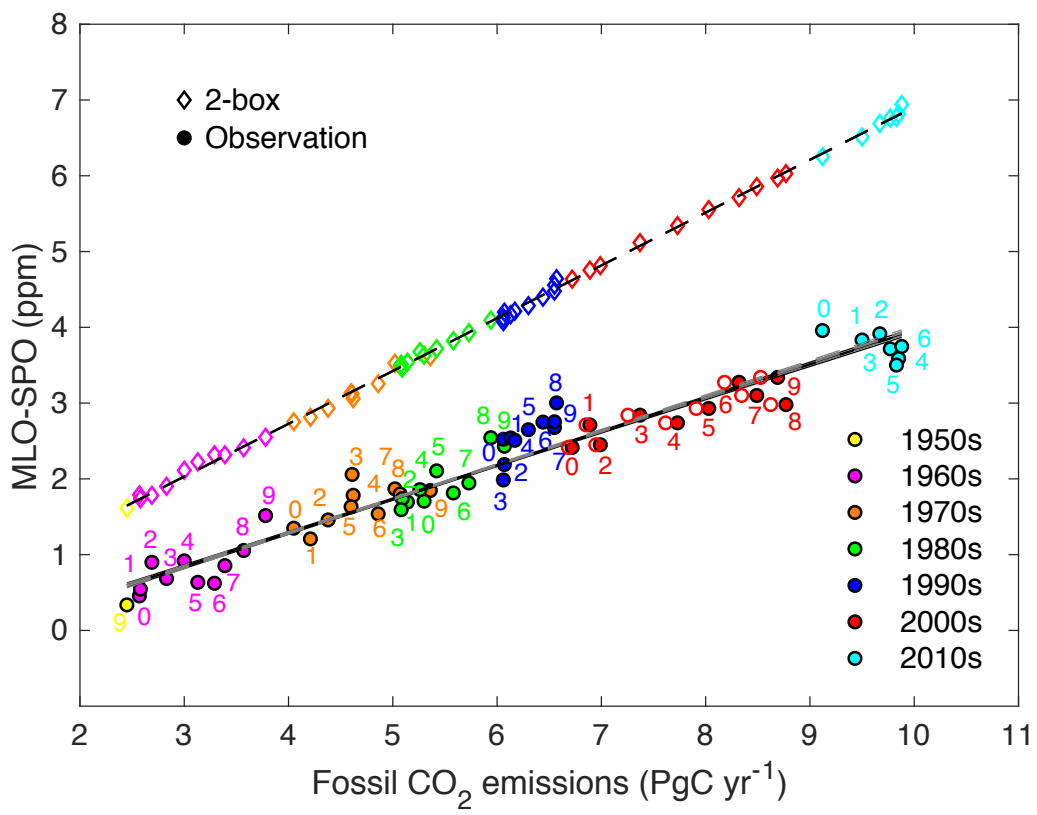
Figure ED6. Trend in ‘rectifier inter-hemispheric CO₂ gradient’ simulated with TM3 related to the trend of atmospheric transport convoluted by trends in the seasonal amplitude and phase of land-atmosphere fluxes. Scatter diagram of simulated IG changes with TM3 and ERA-interim wind fields (see Methods) related to the trend of atmospheric transport convoluted by trends in the seasonal amplitude and phase of land-atmosphere fluxes, called ‘trend in rectifier’. The results are obtained by applying TM3 to variable maps of seasonal land fluxes created by subtracting the mean seasonal cycle and the long-term mean from the inverted land fluxes (at every grid cell). Then, the simulated CO₂ field was sampled at the same location than each long-term station, and the difference from SPO is plotted as IG due to ‘trend in rectifier’. The absence of any trend in IG from ‘trend in rectifier’ related mechanisms, suggests that this process does not explain any trend in the observed IG that would be aliased to trends in L_N in the 2-box inversion.

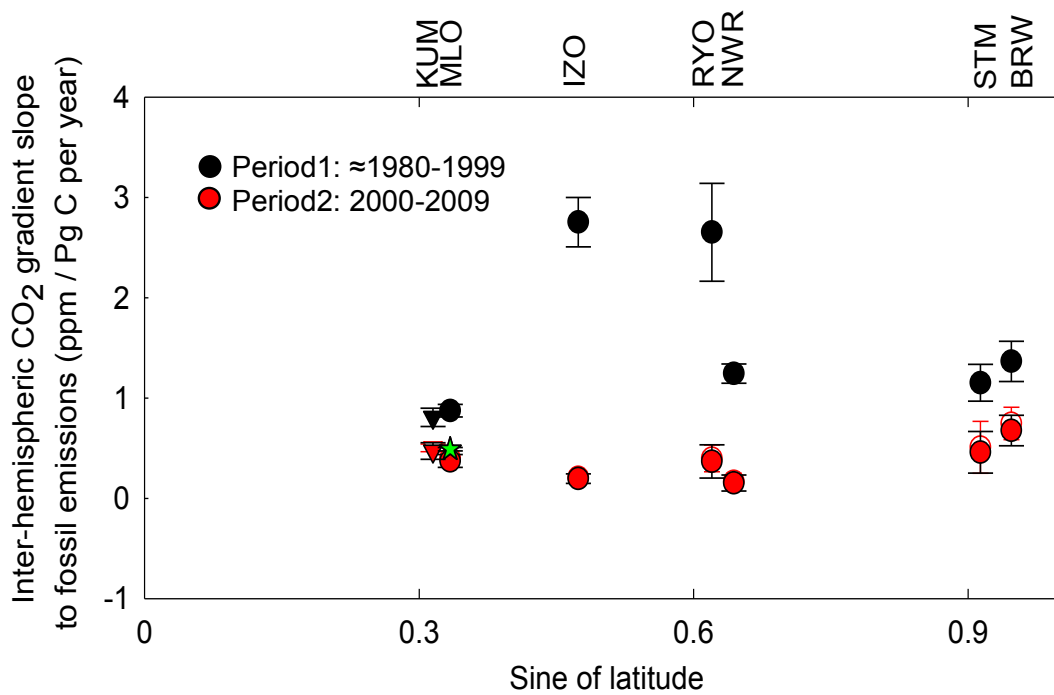
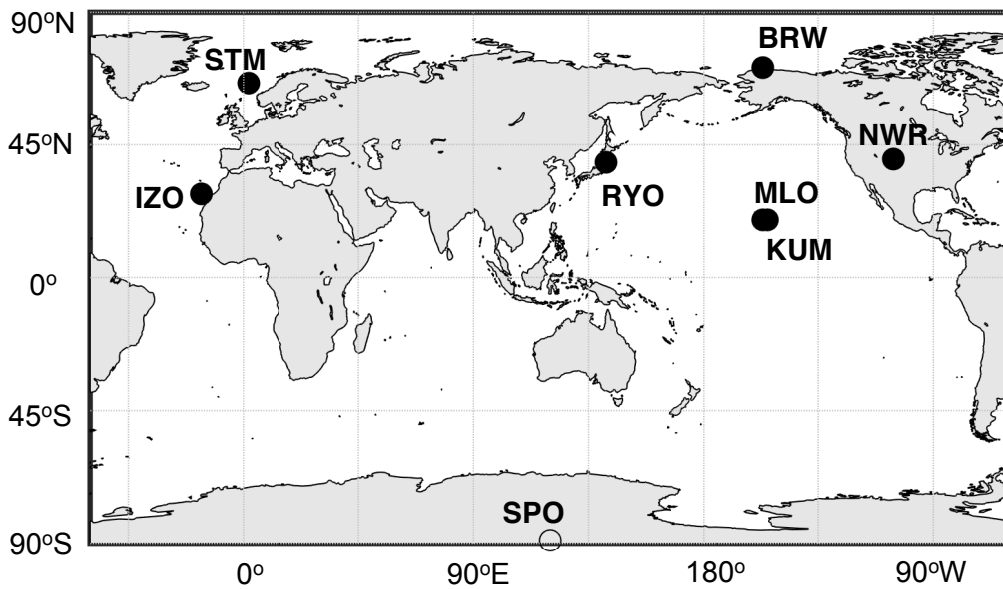
Figure ED7. Northern land sink simulated by different land carbon cycle models. **a.** Northern land sink from Trendy V2 ensemble (1959-2012), **b.** from TRENDY V4 ensemble used in this study (1959-2014), **c.** MsTMIP ensemble with models considering nitrogen deposition change (1959-2010), **d.** MsTMIP ensemble with models not considering nitrogen deposition change (1959-2010). MsTMIP models having CO₂ sources in the Northern Hemisphere and / or global land sink outside observed range were not used.

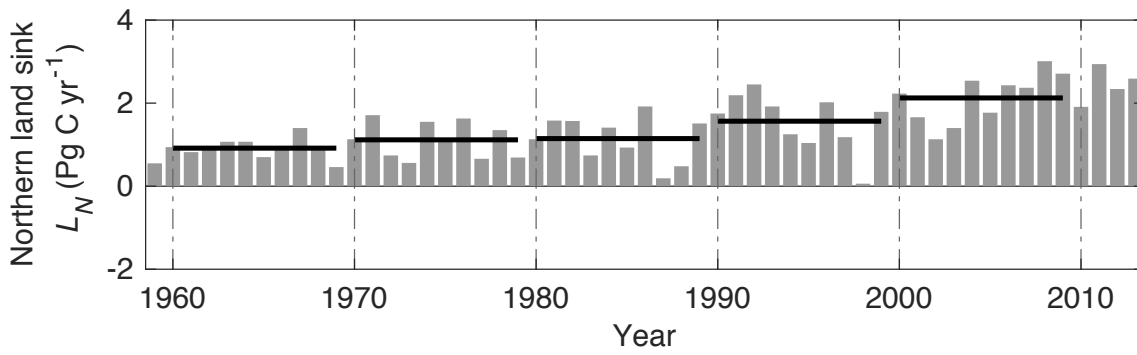
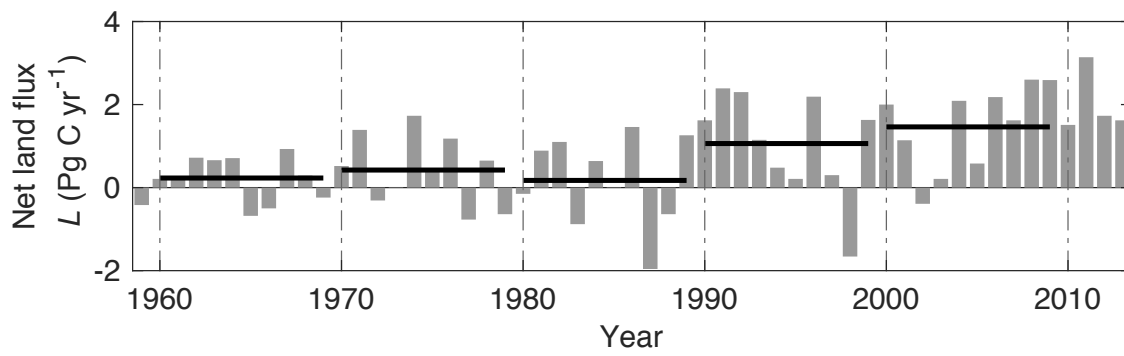
Table ED1. Atmospheric stations with long term CO₂ records since the early 1980s. The 7 stations used in the analysis are listed on top. The 4 stations in red did not have a regression slope of their CO₂ difference to SPO (IG) with respect to fossil fuel emissions with a $r^2 > 0.3$ during either period 1 (1980–1989) or period 2 (1990–1999). The MLO station from NOAA ESRL (in italics) was not used but the longer Scripps record instead.

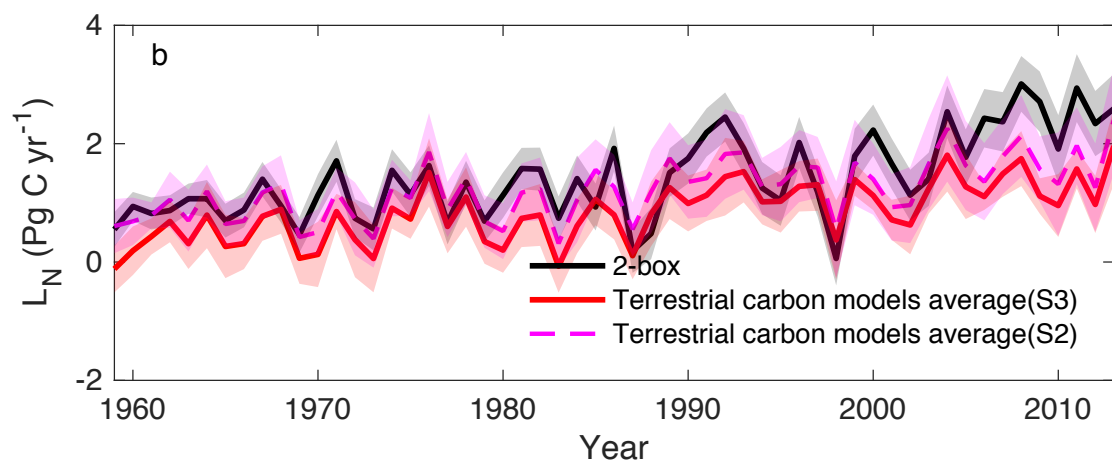
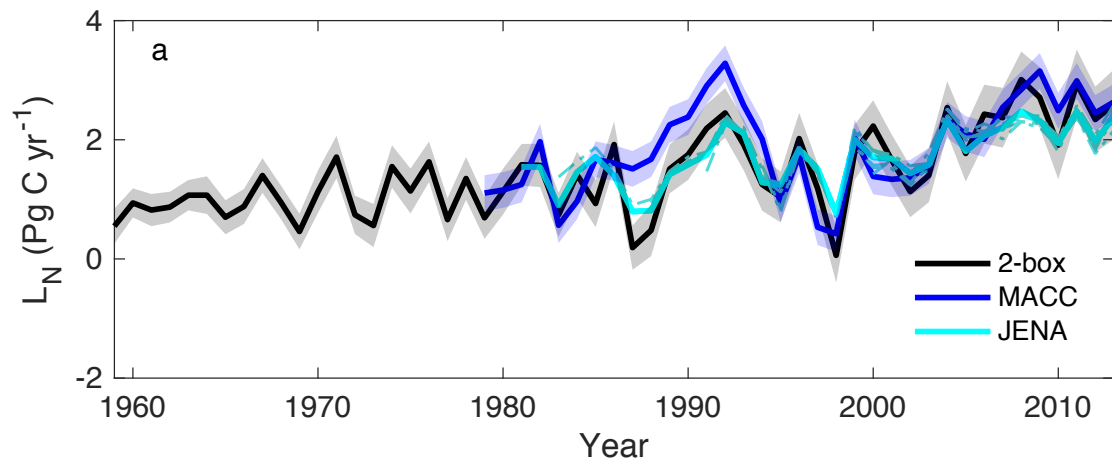
Table ED2. Linear regression slopes of the inter-hemispheric CO₂ gradient versus fossil fuel emissions at long-term atmospheric stations. Slopes at the long-term stations are given for period 1 (1980–1989 and 1990–1999) and period 2 (2000–2009). All slope values are in ppm per PgC yr⁻¹. Uncertainties on the slopes are 1-sigma in parenthesis. Red numbers are stations with $r^2 < 0.3$ for which the slope was not calculated (N/A)

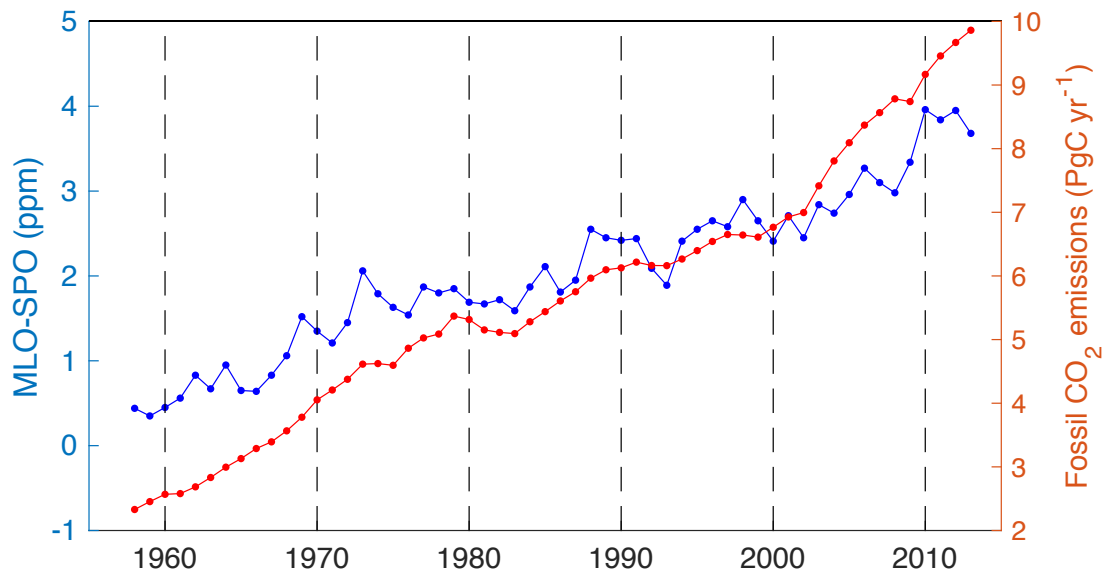
Table ED3. Summary of estimates of northern land sink **a.** Decadal mean and long-term mean fossil fuel emissions, net land sink and northern land sink over the last 5 decades. **b.** Decadal mean in northern land sink from Trendy V4 land carbon cycle models.

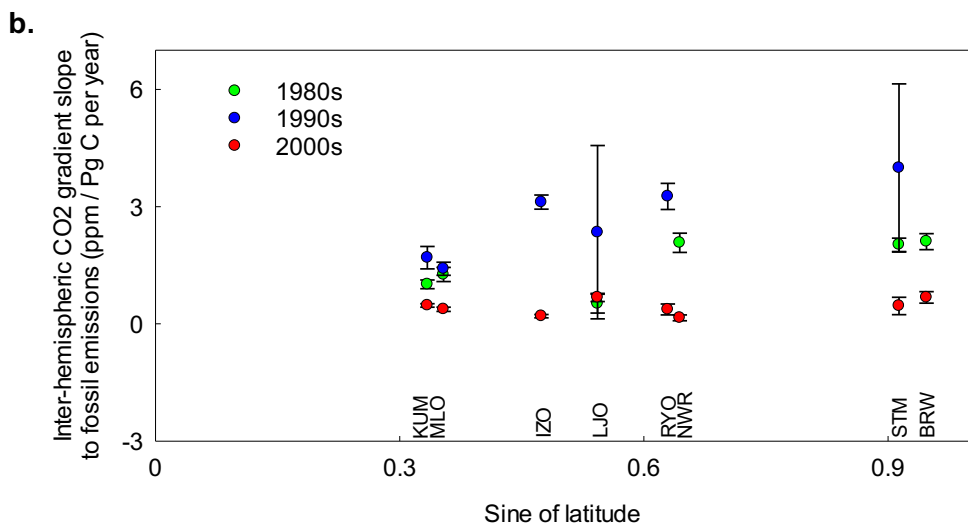
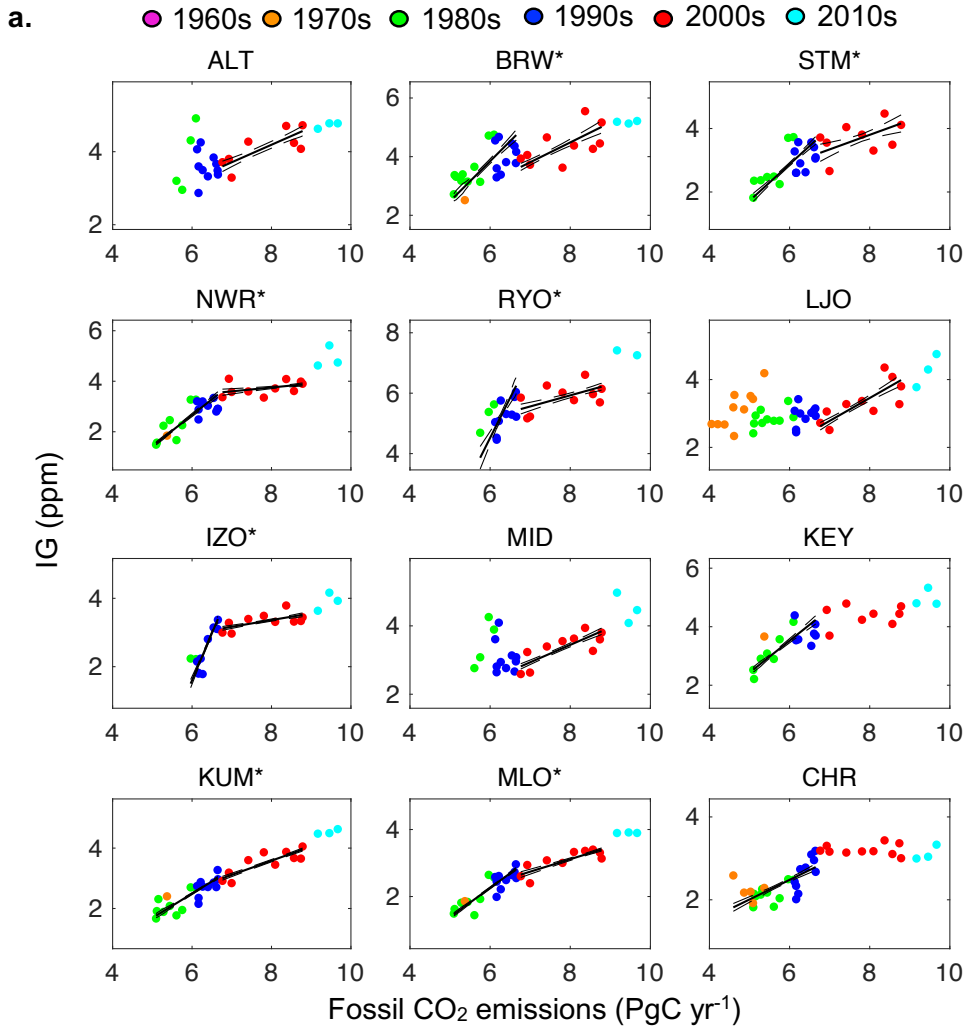


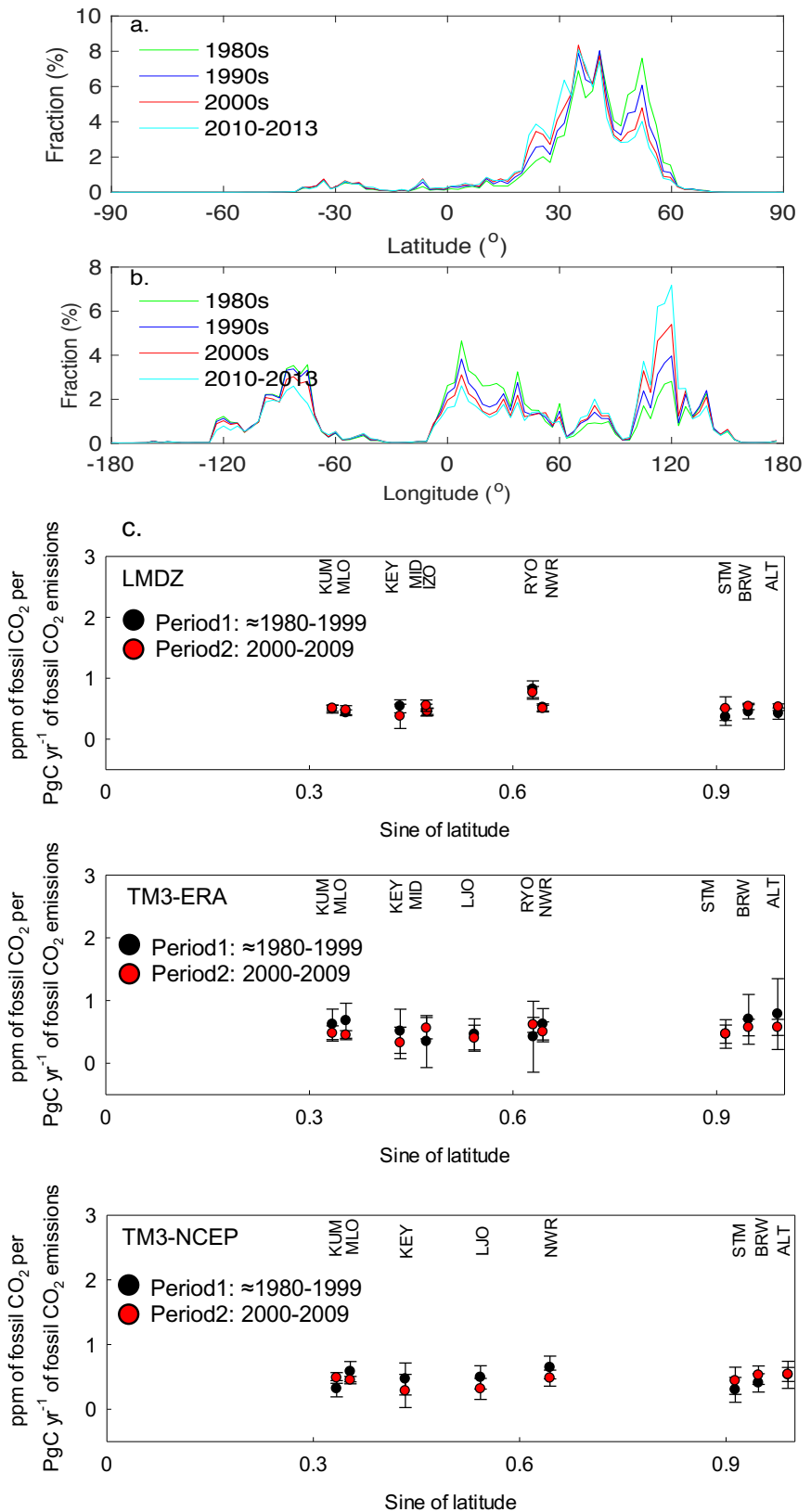


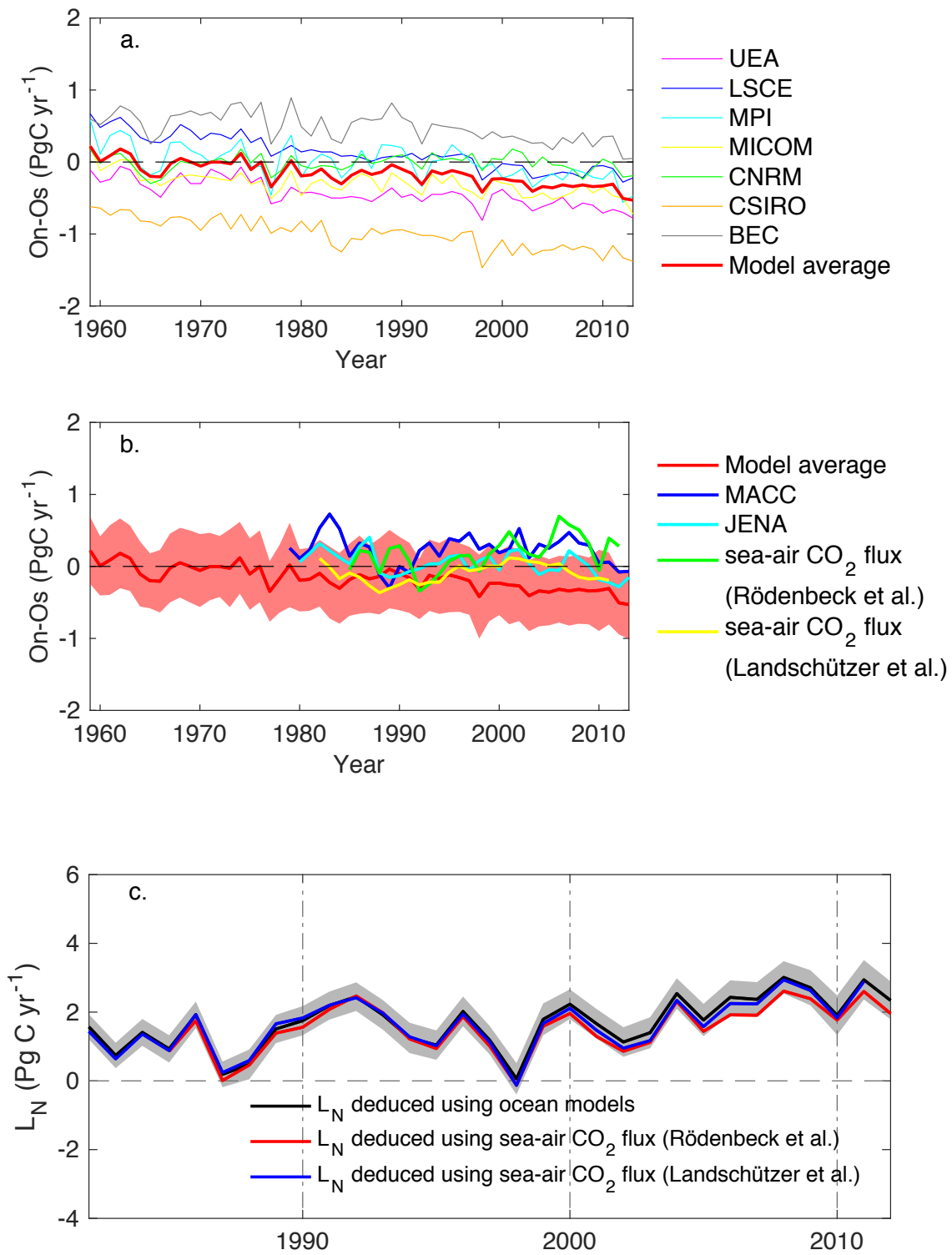


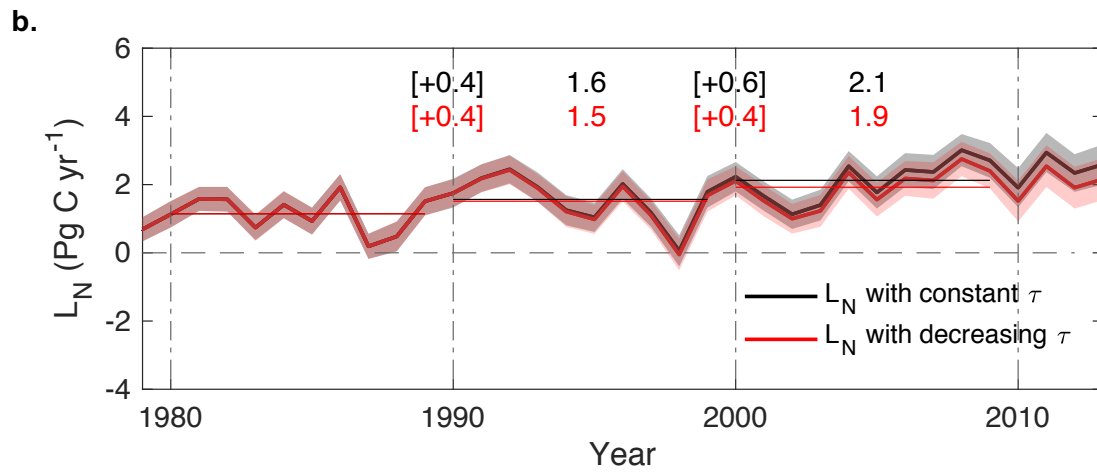
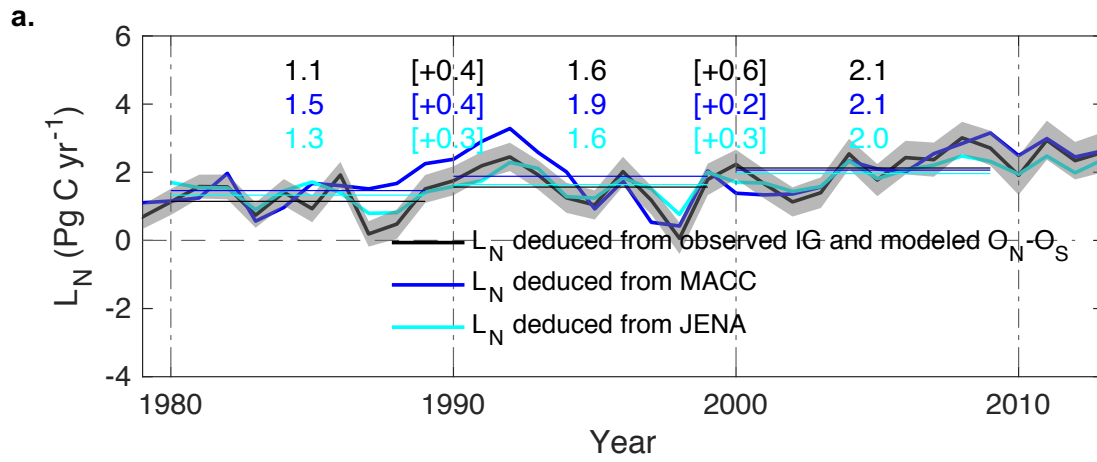




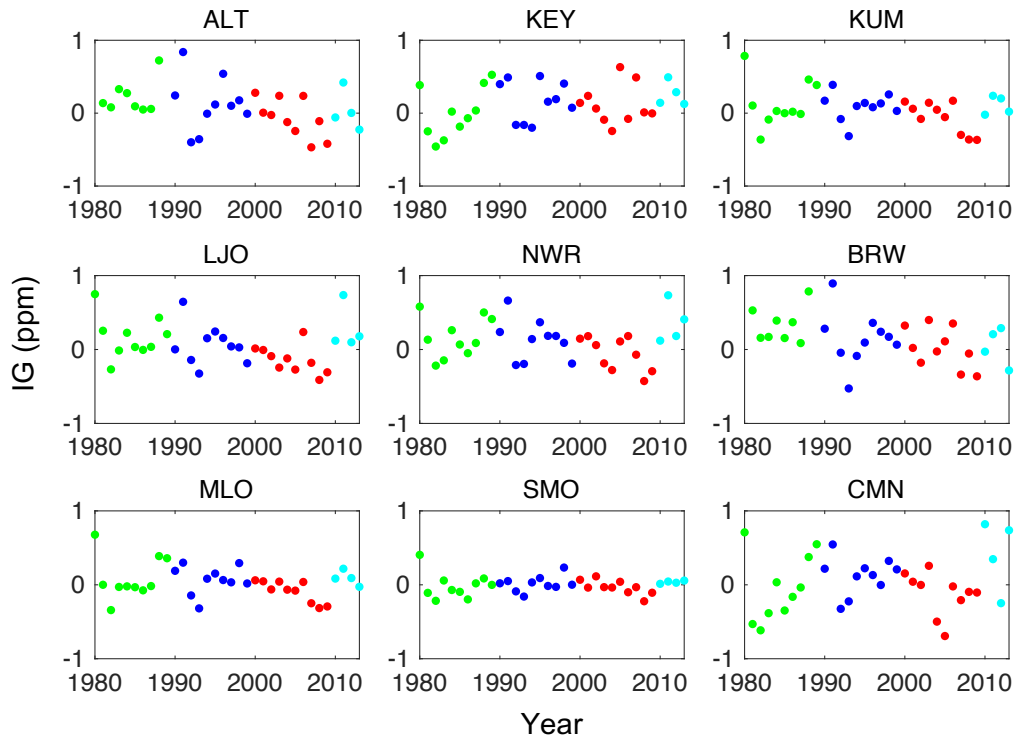


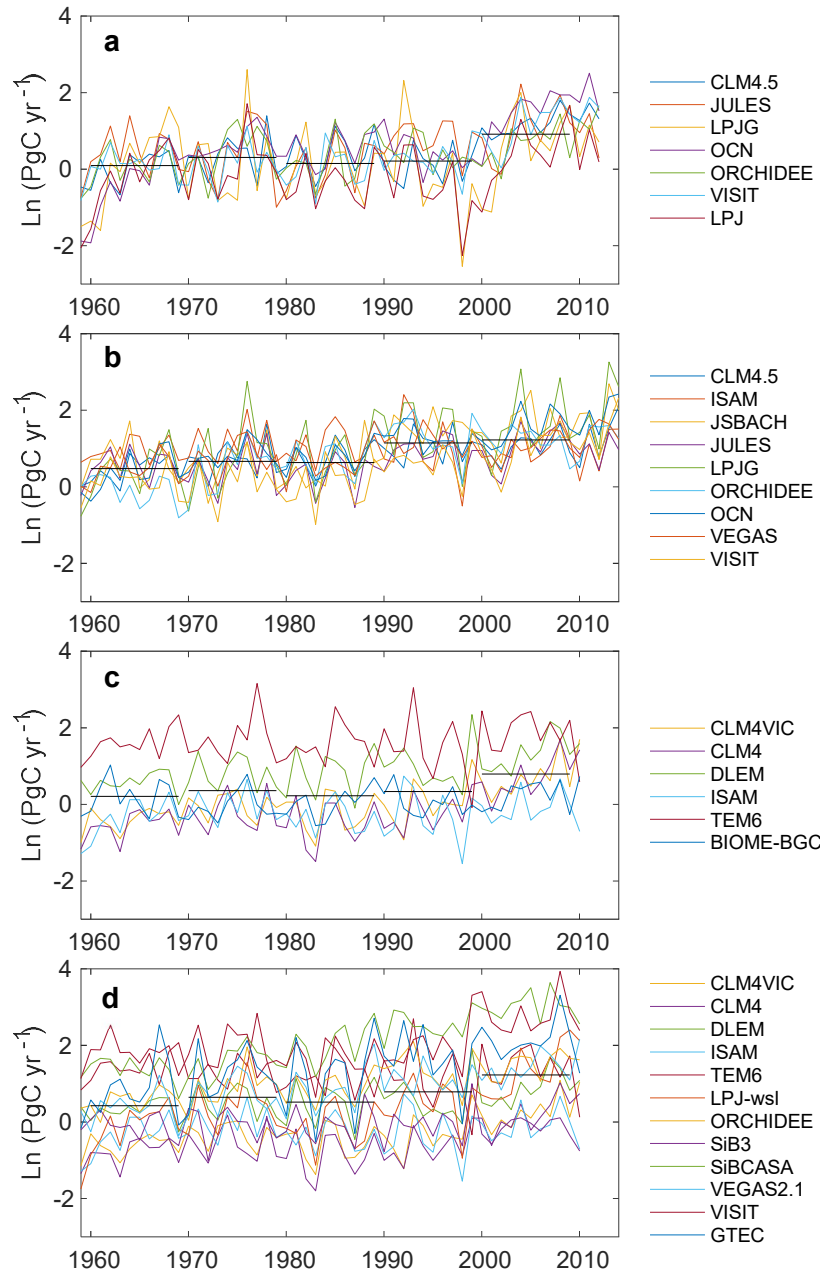






● 1980s ● 1990s ● 2000s ● 2010s





Site	Lat	Lon	Type	Network	Start year	End year	Slope	Std.
BRW	71.3	-156.6	continuous	NOAA ESRL	1979	2012	0.49	0.04
STM	66	2	flask	NOAA ESRL	1982	2008	0.57	0.05
NWR	40.1	-105.6	flask	NOAA ESRL	1979	2012	0.66	0.04
RYO	39	141.8	continuous	NOAA ESRL	1987	2012	0.58	0.05
IZO	28.3	-16.5	continuous	NOAA ESRL	1988	2012	0.51	0.04
KUM	19.5	-154.8	flask	NOAA ESRL	1979	2012	0.59	0.02
MLO	19.5	-155.6	continuous	Scripps	1958	2013	0.49	0.01
<i>MLO</i>	<i>19.5</i>	<i>-155.6</i>	<i>continuous</i>	<i>NOAA ESRL</i>	<i>1979</i>	<i>2012</i>	<i>0.49</i>	<i>0.02</i>
ALT	82.5	-62.5	flask	NOAA ESRL	1986	2012	0.36	0.04
LJO	32.9	-117.3	flask	Scripps	1969	2012	0.22	0.03
MID	28.2	-177.4	flask	NOAA ESRL	1986	2012	0.36	0.05
KEY	25.7	-80.2	flask	NOAA ESRL	1979	2012	0.49	0.04

Site	Latitude	Slope from ODR (1 σ)		Correlation coefficient (R)	
		Period 1 1980s and 1990s	Period 2 2000s	Period 1 1980s and 1990s	Period 2 2000s
ALT	82.5	N/A	0.48 (0.10)	0.04	0.76
BRW	71.3	1.37 (0.20)	0.68 (0.15)	0.66	0.60
STM	66	1.15 (0.15)	0.46 (0.25)	0.67	0.43
NWR	40.1	1.24 (0.10)	0.15 (0.07)	0.81	0.39
RYO	39	2.65 (0.40)	0.37 (0.11)	0.54	0.51
LJO	32.9	N/A	0.67 (0.11)	-0.03	0.75
IZO	28.3	2.75 (0.32)	0.20 (0.04)	0.86	0.62
MID	28.2	N/A	0.51 (0.09)	-0.21	0.78
KEY	25.7	1.09 (0.11)	N/A	0.72	0.21
KUM	19.5	0.81 (0.07)	0.47 (0.06)	0.82	0.83
MLO	19.5	0.87 (0.06)	0.37 (0.06)	0.87	0.82

a.

		1960s	1970s	1980s	1990s	2000s	2010-2013	1960-2013
Fossil emissions	<i>F</i>	3.1 ± 0.2	4.7 ± 0.3	5.5 ± 0.3	6.4 ± 0.33	7.9 ± 0.4	9.5 ± 0.5	5.8 ± 0.3
Net land sink	<i>L</i>	0.2 ± 0.6	0.4 ± 0.6	0.2 ± 0.6	1.1 ± 0.6	1.5 ± 0.7	2.0 ± 0.7	0.8 ± 0.6
Northern land sink	<i>L_N</i>	0.9 ± 0.3	1.1 ± 0.4	1.1 ± 0.4	1.6 ± 0.4	2.1 ± 0.5	2.4 ± 0.6	1.4 ± 0.4
	<i>L_{N MACC}</i>			1.5 ± 0.3	1.9 ± 0.3	2.1 ± 0.3	2.6 ± 0.3	
	<i>L_{N JENA}</i>			1.3	1.6	2.0	2.2	
	<i>L_{N mod}</i>	0.5 ± 0.3	0.7 ± 0.3	0.6 ± 0.3	1.1 ± 0.3	1.2 ± 0.2	1.4 ± 0.4	0.9 ± 0.2

b.

Northern land sink in Land carbon models (TRENDY v4)							
	1960s	1970s	1980s	1990s	2000s	2010-2013	
ISAM	0.9	1.1	1.1	1.0	1.1	0.8	
JULES	0,6	0,5	0,3	0,9	1,0	1,0	
JSBACH	0,7	0,6	0,5	1,5	1,5	1,8	
VEGAS	0,5	0,8	0,7	1,2	1,0	1,4	
ORCHIDEE	-0,1	0,5	0,8	1,3	1,2	1,4	
LPJ GUESS	0,5	0,8	0,8	1,4	1,6	1,9	
VISIT^a	0,2	0,1	0,0	0,7	1,0	1,2	
OCN^a	0,4	0,8	0,7	1,3	1,5	1,8	
CLM4.5^a	0,4	0,7	0,7	1,0	1,1	1,1	
Mean of models (± std.)	0.5 ± 0.3	0.7 ± 0.3	0.6 ± 0.3	1.1 ± 0.3	1.2 ± 0.2	1.4 ± 0.4	